Nano Research

ISSN 1998-0124 CN 11-5974/O4
https://doi.org/10.26599/NR.2026.94909204

Research Article

Monolithically integrated flexible multimodal healthcare electronics on perovskite piezoelectric thin film for human motion and physiological signal monitoring

Mookyum Kim[1], Kangsan Lee[2,3], Myeong Seok Ko[2,3], Il Doh[2,4], Seong-Gu Hong[2,3,5](✉)

[1] Department of Bio-Healthcare, Hwasung Medi-Science University, Gyeonggi-do 18274, Republic of Korea

[2] Department of Precision Measurement Engineering, University of Science and Technology, Daejeon 34113, Republic of Korea

[3] Convergence Research Center for Meta-Touch, Korea Research Institute of Standards and Science, Daejeon 34113, Republic of Korea

[4] Division of Biomedical Metrology, Korea Research Institute of Standards and Science, Daejeon 34113, Republic of Korea

[5] Division of Chemical and Material Metrology, Korea Research Institute of Standards and Science, Daejeon 34113, Republic of Korea

Nano Res., **Just Accepted Manuscript** • https://doi.org/10.26599/NR.2026.94909204

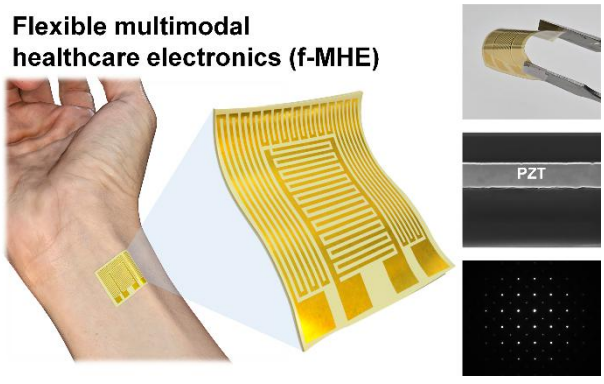
https://www.sciopen.com/journal/1998-0124 on Sep. 19, 2026

© The Authors(s)

Just Accepted

This is a "Just Accepted" manuscript, which has been examined by the peer-review process and has been accepted for publication. A "Just Accepted" manuscript is published online shortly after its acceptance,which is prior to technical editing and formatting and author proofing. Tsinghua University Press (TUP) provides "Just Accepted" as an optional and free service which allows authors to make their results available to the research community as soon as possible after acceptance. After a manuscript has been technically edited and formatted, and the page proofs have been corrected, it will be removed from the "Just Accepted" web site and published officially with volume and article number (e.g., *Nano Research*, **2025**, *18*, 94906990). Please note that technical editing may introduce minor changes to the manuscript text and/or graphics which may affect the content, and all legal disclaimers that apply to the journal pertain. In no event shall TUP be held responsible for errors or consequences arising from the use of any information contained in these "Just Accepted" manuscripts. To cite this anuscript please use its Digital Object Identifier (DOI®),which is identical for all formats of publication.

Just Accepted



Monolithically integrated flexible multimodal healthcare electronics (f-MHE) are developed on a perovskite piezoelectric thin film for simultaneous pressure and temperature sensing. This single-layer platform enables efficient monitoring of human motion and physiological signals with minimal cross-sensitivity between the pressure and temperature sensing channels, while offering high sensitivity, durability, and conformability for real-time health tracking and personalized monitoring applications.

Just Accepted

Nano Research

Open Access

Research Article

Monolithically integrated flexible multimodal healthcare electronics on perovskite piezoelectric thin film for human motion and physiological signal monitoring

Mookyum Kim[1], Kangsan Lee[2,3], Myeong Seok Ko[2,3], Il Doh[2,4], and Seong-Gu Hong[2,3,5]

[1] *Department of Bio-Healthcare, Hwasung Medi-Science University, Gyeonggi-do 18274, Republic of Korea*
[2] *Department of Precision Measurement Engineering, University of Science and Technology, Daejeon 34113, Republic of Korea*
[3] *Convergence Research Center for Meta-Touch, Korea Research Institute of Standards and Science, Daejeon 34113, Republic of Korea*
[4] *Division of Biomedical Metrology, Korea Research Institute of Standards and Science, Daejeon 34113, Republic of Korea*
[5] *Division of Chemical and Material Metrology, Korea Research Institute of Standards and Science, Daejeon 34113, Republic of Korea*

Received: 19 May 2026; **Revised:** 3 August 2026; **Accepted:** 19 September 2026

Address correspondence to sghong@kriss.re.kr

Cite this article: *Nano Research*, 2026, 19, 94909204 https://doi.org/10.26599/NR.2026.94909204

ABSTRACT: Integrating multiple sensing modalities into a compact, mechanically compliant platform is essential for wearable healthcare electronics aimed at monitoring human motion and physiological signals. However, conventional multimodal sensors typically rely on rigid, multilayered architectures that limit flexibility, increase fabrication complexity, and introduce mechanically vulnerable interfacial boundaries. Here, we present a monolithically integrated flexible multimodal healthcare electronics (f-MHE) platform fabricated on a perovskite piezoelectric thin film, enabling dual-parameter detection of pressure and temperature within a single-layer architecture. The platform integrates an interdigitated-electrode piezoelectric pressure sensor for pulse-wave detection and a serpentine thermoresistive temperature sensor for skin-temperature measurement. The monolithic design eliminates multilayer stacking and repeated alignment/etching steps, thereby simplifying fabrication, reducing interfacial boundaries, and enhancing mechanical integrity. As a result, the f-MHE achieves an ultrathin (<5 μm), mechanically compliant form factor that enables conformal attachment to curved and deformable surfaces, including human skin. The device exhibits a pressure sensitivity of 24.1 mV kPa^{-1} with a resolution of <0.1 kPa over 0.1–25 kPa, and a temperature sensitivity of 5.03 Ω $°C^{-1}$ with a resolution of <0.1 °C over 25–45 °C. Robust linearity, stability, and durability are maintained under repeated mechanical deformation. Multimodal sensing is further validated through real-time, simultaneous monitoring of pulse waves, respiration, and body motion. This work provides a structurally simple yet highly efficient and reliable strategy for multifunctional sensor integration and highlights the potential of monolithic thin-film platforms for next-generation wearable health monitoring.

KEYWORDS: multimodal sensing, wearable healthcare electronics, physiological signals, microfabrication, monolithic integration, perovskite piezoelectric thin film

1 Introduction

The rapid advancement of digital healthcare technologies has accelerated the integration of biomedical devices into daily life [1–2]. Wearable devices are particularly suitable for personalized health monitoring and early disease detection because they enable noninvasive, continuous sensing of physiological signals through the skin [3–8]. For accurate health-status assessment, simultaneous monitoring of multiple physiological parameters is often required, which demands sensor systems that provide stable signals over extended periods while maintaining user comfort. Despite remarkable advances, commercial devices such as smartwatches still exhibit limited wearability due to their rigid form factors [9–11]. Their rigidity confines use largely to the wrist and can reduce usability during complex or dynamic movements. Moreover, stiffness mismatch between rigid devices and soft skin can cause discomfort and degrade signal reliability during long-term wear. In addition, many conventional devices are designed to measure only a single parameter, limiting their ability to capture multiple signals concurrently [12–14].

To address these limitations, extensive efforts have focused on flexible sensor technologies using skin-compatible materials [15–24]. Flexible electronics can conform to curved and deformable surfaces, improving signal fidelity and enabling sensing on dynamic, irregular geometries [25–33]. Accordingly, flexible multifunctional sensor systems capable of detecting multiple signals with high sensitivity have attracted considerable interest. However, many previous multimodal platforms adopt multilayer architectures that require sequential stacking of individual sensing components, together with selective etching and repeated alignment. These processes increase fabrication complexity and can reduce manufacturing yield. Moreover, increased device thickness compromises flexibility and conformability. Critically, stiffness mismatch among stacked layers can concentrate stress at interfaces and trigger premature failures such as interfacial delamination, thereby degrading mechanical durability [34]. Therefore, integrating multiple

Just Accepted

sensing functions within a single-layer configuration is an effective strategy to simplify fabrication, minimize thickness, and improve mechanical reliability in flexible electronics.

In this study, we develop a flexible multimodal healthcare electronics (f-MHE) platform in which a piezoelectric pressure sensor and a thermoresistive temperature sensor are monolithically integrated on a perovskite piezoelectric thin film, enabling simultaneous pressure and temperature sensing. Unlike conventional multilayer configurations, the monolithic design allows the pressure- and temperature-sensing elements to be patterned within a unified thin-film layer, eliminating repeated alignment and etching steps otherwise required for stacking discrete sensor layers. This simplification improves fabrication efficiency and manufacturing yield. Moreover, the compact single-layer structure reduces the overall thickness, enhancing flexibility and conformability to curved, dynamic surfaces such as human skin and enabling sensitive detection of subtle skin-originated signals. The piezoelectric pressure sensor is based on a lead zirconate titanate ($Pb(Zr,Ti)O_3$, PZT) thin film and enables self-powered operation by converting mechanical stimuli into electrical signals without an external power source. The thermoresistive temperature sensor employs finely micropatterned Au/Cr structures to achieve a linear and reliable thermal response within the physiological temperature range. We first characterize the pressure- and temperature-sensing performances separately and then demonstrate low-crosstalk multimodal sensing through physiological and human-motion experiments.

2 Experimental

2.1 Preparation of perovskite PZT thin film

A PZT sol–gel precursor solution (QTS-PZT52/48, Quintess Co., Ltd., Republic of Korea) was spin-coated onto a double-side polished 2-inch sapphire wafer (c-plane (0001), Hi-Solar Co., Ltd., Republic of Korea) at 2,000 rpm for 30 s using a spin coater (NSF-1500P, Rhabdos Co., Ltd., Republic of Korea). Following each spin-coating step, the film was heat-treated at 450 °C for 30 min in air using a high-temperature furnace (SH-FU-14MG, SH Scientific Co., Ltd., Republic of Korea). This spin-coating/heat-treatment cycle was repeated 10 times to obtain a target thickness of 1 μm. Finally, the film was crystallized at 700 °C for 2 h in air using the same high-temperature furnace, yielding a crystalline perovskite PZT thin film.

2.2 Fabrication of f-MHE

A 10 nm-thick Cr adhesion layer and a 100 nm-thick Au layer were sequentially deposited on the PZT film/sapphire wafer using an electron-beam evaporator (custom-built, IVT Korea Co., Ltd., Republic of Korea) at a deposition rate of 0.3 Å s^{-1} under a base pressure of 5×10^{-7} Torr. The Au/Cr metal layer was then simultaneously patterned into interdigitated electrodes for the piezoelectric pressure sensor and serpentine structures for the thermoresistive temperature sensor using photolithography with an ultraviolet (UV) mask aligner (MDA-400M, MIDAS System Co., Ltd., Republic of Korea). Subsequently, a polymethyl methacrylate (PMMA) passivation layer (A11, Kayaku Advanced Materials, Inc., United States) was spin-coated onto the sapphire/PZT/Cr–Au (patterned) stack. To separate the device stack from the sapphire carrier, an excimer laser system (KORONA, AP Systems Corp., Republic of Korea) was irradiated onto the backside of the sapphire wafer (wavelength of 308 nm, pulse energy of 600 mJ $shot^{-1}$, pulse duration of 25 ns, energy density of 469 mJ cm^{-2}), resulting in the release of the PZT/Cr–Au (patterned)/PMMA stack. The released stack was then transferred onto a 2.6 μm-thick polyethylene terephthalate (PET) substrate (Single-Sided Adhesive Tape, Horaetape, China) using a UV-release dicing tape (AU170, AMC Co., Ltd., Republic of Korea). The tape was removed by UV exposure for 100 s. Next, via-holes were opened at the electrode-pad regions by oxygen-plasma reactive ion etching using a reactive ion etcher (Asher, SNTEK Co., Ltd., Republic of Korea) with an O_2 flow rate of 50 sccm and a radio frequency power of 100 W, followed by electrical wiring to the exposed pads. Finally, the PZT thin film was poled to enhance piezoelectric properties by aligning ferroelectric dipoles under an electric field of 150 kV cm^{-1} at 85 °C for 6 h while immersed in fluorocarbon oil (Fluorinert Electronic Liquid, 3M, United States).

2.3 Morphological, structural, and chemical characterization

The morphology and dimensions of the fabricated f-MHE were examined using bright-field optical microscopy (BX53M, Olympus Corp., Japan) and field-emission scanning electron microscopy (SEM) (NX5000 Ethos, Hitachi High-Tech Corp., Japan) operated at an accelerating voltage of 5 kV. The surface roughness and thickness uniformity of the PZT thin film were evaluated by atomic force microscopy (AFM) (MFP-3D, Oxford Instruments plc, United Kingdom) using a cantilever tip with a spring constant of 68 N m^{-1}; measurements were performed at a scan rate of 0.1–0.5 Hz with a set-point of 680 mV.

Crystallographic and structural information was obtained by transmission electron microscopy (TEM) (JEM-2100F, JEOL Ltd., Japan) operated at 200 kV (spatial resolution of 0.1 nm) and Raman spectroscopy (LabRAM HR, Horiba, Ltd., Japan) using a 514 nm excitation laser over 100–1100 cm^{-1}. The crystalline structure and phase composition of the PZT film were analyzed by X-ray diffraction (XRD) (SmartLab, Rigaku Corp., Japan) with a 2θ scan from 20° to 80°. Surface chemical composition and oxidation states were investigated by X-ray photoelectron spectroscopy (XPS) (Nexsa G2, Thermo Fisher Scientific Inc., United States) using a monochromatic Al Kα source, with binding energies calibrated to the C 1s peak at 285.0 eV.

2.4 Performance characterization of f-MHE

To evaluate the pressure-sensing performance of the fabricated f-MHE, pressures ranging from 0 to 45 kPa were applied in 0.1 kPa increments using a custom-built pressure simulator consisting of a pulse simulator, a portable pneumatic pressure calibrator (PCS-P100, PDK Co., Ltd., Republic of Korea), and an arm-mimicking phantom. The piezoelectric output voltage was recorded with a multifunction data-acquisition module (USB-6009, National Instruments, United States). For temperature-sensing performance, a temperature controller (TC01, Multi Channel Systems MCS GmbH, Germany) was used to maintain the physiological temperature range of 25–45 °C with a set-point resolution of 0.1 °C. The resistance of the thermoresistive sensor was measured with a

Just Accepted

digital multimeter (Keithley 2010 Multimeter, Tektronix, United States). Pressure-induced voltage and temperature-dependent resistance signals were acquired in real-time using a custom-built data acquisition system based on LabVIEW (2021 SP1, National Instruments, United States).

2.5 Human-subject experiments

All experiments involving a human participant were conducted in accordance with a protocol approved by the Public Institutional Review Board designated by the Ministry of Health and Welfare of the Republic of Korea (IRB No. 2026-2055-001). Written informed consent was obtained from the participant prior to participation. All human-subject experiments, including the finger-, neck-, face-mask-, and wrist-mounted measurements, were performed on one healthy 30-year-old male participant.

3 Results and discussion

3.1 Design and fabrication of f-MHE

We designed a flexible multimodal healthcare electronics system capable of simultaneous pressure and temperature sensing based on an integrated thin-film architecture (Fig. 1(a)). The device combines a piezoelectric pressure sensor with interdigitated electrodes and a thermoresistive temperature sensor with a micropatterned serpentine geometry within a single-layer platform. This monolithic configuration enables multifunctional sensing in a compact form factor and eliminates multilayer stacking as well as complex photolithographic alignment steps. By removing these steps, the device structure is simplified, which improves fabrication efficiency and manufacturing yield while reducing the overall thickness. The reduced thickness enhances mechanical flexibility and conformability, enabling conformal attachment to curved and deformable surfaces, including human skin; such conformal contact helps maintain a stable skin–device interface and supports reliable signal acquisition over extended periods. Moreover, the single-layer architecture suppresses mechanically induced damage at interfacial boundaries under deformation—an issue commonly observed in multilayer devices where stiffness mismatch concentrates stress at interfaces—thereby improving long-term durability [34].

The device consists of a PET flexible substrate, a perovskite-phase PZT thin film, a micropatterned Au/Cr layer that serves as the pressure-sensing electrodes and the thermoresistive element, and a PMMA passivation layer (Fig. 1(b)). The PET substrate provides compliant mechanical support, whereas the PZT film provides piezoelectric functionality and contributes to structural integrity. The pressure sensor is positioned at the center of the device, while the temperature sensor is arranged along the periphery, enabling spatial separation and minimizing cross-interference between the two sensing modalities.

Figure 1(c) illustrates the fabrication process. The PZT film was fabricated on a sapphire wafer via repeated sol–gel coating and thermal processing, followed by high-temperature crystallization. The Au/Cr layer was deposited and patterned to define both the interdigitated electrodes and serpentine thermoresistive structures, after which the PMMA passivation layer was coated. The resulting PZT/Cr–Au (patterned)/PMMA stack was released from the sapphire carrier by a laser lift-off process (Fig. S1 in the ESM) and transferred onto a PET substrate [35,36]. Finally, poling was performed at 150 kV cm^{-1} and 85 °C to align ferroelectric dipoles and enhance piezoelectric performance.

Figure 1(d) shows a top-view photograph of the fabricated device with an active sensing area of 18 mm × 16 mm (length × width). It includes interdigitated electrodes for pressure sensing with a line width and gap of 100 μm, and serpentine Au/Cr traces for temperature sensing with a line width of 100 μm and a total length of 700 mm. Figure 1(e) demonstrates mechanical flexibility, showing that the device can be bent without visible damage or delamination. The cross-sectional SEM image in Fig. 1(f) confirms the multilayer stack, which includes a 1.2 μm-thick PMMA layer, a 110 nm-thick Au/Cr layer, a 1.0 μm-thick PZT layer, and a 2.6 μm-thick PET substrate, with an overall device thickness of <5 μm. The well-controlled thickness of each layer supports the reproducibility of the fabrication process and provides a mechanically robust structure suitable for wearable operation.

3.2 Morphological, structural, and chemical properties of PZT thin film

The structural integrity, crystallinity, and perovskite phase formation of the fabricated PZT film were examined using various analytical techniques. As shown in Fig. 2(a), the bright-field optical image exhibits a defect-free and crack-free surface, ensuring the structural integrity of the film. Additionally, the uniform color across the entire surface of the film indicates that light is uniformly reflected or transmitted, suggesting that the film's thickness and surface properties are consistent throughout.

Figure 2(b) presents AFM measurements of the PZT film. The root mean square roughness of the surface was 0.18 nm, indicating a highly planar surface morphology with minimal topographical variation. The height profile along the red line in the left panel of Fig. 2(b) further supports this result, showing negligible height fluctuations of <1 nm and confirming the uniform thickness of the film.

Figure 2(c) presents a TEM selected-area electron diffraction (SAED) pattern of the PZT thin film, revealing the structural features of the crystalline lattice [37,38]. The results confirm the uniformity of the piezoelectric domains and the absence of dislocations, displaying a perovskite structure oriented along the <001> direction, where the periodic arrangement of Pb, Zr, and Ti atoms reflects high crystallinity and precise atomic ordering. These characterizations collectively confirm the formation of a highly crystalline perovskite structure in the PZT film.

Figure 2(d) shows the Raman spectroscopy measurements of the PZT film. The excitation of Raman-active modes serves as a clear indicator of crystallization in the perovskite phase of PZT [39,40]. Distinct peaks were observed at wavenumbers of 140, 200, 270, 330, 600, and 720 cm^{-1}, corresponding to the A1(1TO), E(2TO), E+B1, A1(2TO), E(3TO), E(2LO)+A(2LO), A1(3TO), and E(3LO)+A1(3LO) modes, respectively, all of which are consistent with Raman-active modes of tetragonal perovskite phase.

Figure 2(e) presents the XRD spectrum of the PZT film. Distinct diffraction peaks were observed at 2θ values of 22.1°, 31.3°, 38.5°, 44.9°, 50.4°, and 55.5°, corresponding to the characteristic reflection of perovskite PZT. The strong diffraction intensity from the (110) plane (2θ = 31.3°) confirms a preferential (110) orientation of the film. The observed peak

Just Accepted

positions are consistent with the tetragonal perovskite structure of PZT [40,41]. Furthermore, no diffraction peaks associated with the pyrochlore phase (typically appearing at ~29.3° and ~34.1°) were detected, indicating the formation of the perovskite phase without detectable secondary phases [40].

Figure 2(f) shows the XPS spectrum of the PZT film. Core-level peaks were observed at binding energies of Pb 4f (137.94 eV), Zr 3d (182.34 eV), Ti 2p (457.87 eV), and O 1s (531.06 eV), confirming the presence of Pb, Zr, Ti, and O in the PZT film[40,42].

These results demonstrate the structural integrity, high crystallinity, and phase purity of the fabricated PZT film, highlighting the successful fabrication of a high-quality perovskite PZT film.

3.3 Piezoelectric pressure sensor characterization

The piezoelectric pressure-sensing performance of the f-MHE was characterized using a custom-built pressure simulator (Fig. 3(a)) [43]. The simulator comprises a servo-motor-driven pressure generator, a static pressure calibrator, and a data acquisition system. When pressure is applied to the f-MHE by the pressure simulator, the poled dipoles in the piezoelectric PZT layer are compressed along the thickness direction, generating a piezoelectric potential that appears as an output voltage across the pressure-sensing electrodes (Fig. 3(b)).

To evaluate the sensitivity, resolution, linearity, and operating range of the pressure sensor, its electrical responses were measured under various pressure loadings. Figure 3(c) shows the output voltage signals under periodically varying sinusoidal pressures, applied with increments of 0.1 kPa in the 0.1–1 kPa range, 1 kPa in the 1–20 kPa range, and 5 kPa in the 20–45 kPa range. The sensor exhibited a clear output voltage of 23.9 mV even at 0.1 kPa, indicating a pressure resolution of <0.1 kPa and enabling sensitive detection of subtle pressure variations. In the 0–25 kPa range, the sensor exhibited a high sensitivity of 24.1 mV kPa^{-1} with excellent linearity (R^2 = 0.997). When the applied pressure exceeded 25 kPa, the output voltage decreased and became less stable, resulting in a reduced sensitivity of 4.7 mV kPa^{-1} and lower linearity (R^2 = 0.817). These results indicate that the pressure sensor of the f-MHE provides reliable, high-performance operation within the 0–25 kPa range.

The stability and durability of the pressure sensor were assessed under cyclic loading at 5 kPa and 5 Hz for 100,000 cycles (Fig. 3(d)). The average output voltage was 150.9 ± 0.7 mV during the initial 1–20,000 cycles and remained 153.4 ± 0.4 mV during the final 80,001–100,000 cycles, corresponding to <1.7% variation over the entire test. This result confirms stable sensor performance under prolonged repeated loading, demonstrating excellent operational stability and mechanical reliability.

Because PZT films can exhibit a pyroelectric response under transient temperature changes [44,45], the potential influence of pyroelectricity on the pressure-sensor output was also investigated. The f-MHE was placed on a heating plate without externally applied mechanical loading and subjected to three heating and cooling cycles between 25 and 35 °C. As shown in Fig. S2 in the ESM, the thermoresistive temperature sensor exhibited a resistance change of approximately 48.6 Ω during each heating or cooling cycle, corresponding to a temperature variation of approximately 10 °C. By contrast, the maximum voltage generated by the PZT pressure sensor was only approximately 3 mV, and no reproducible voltage response synchronized with the repeated heating and cooling cycles was observed. Considering the pressure sensitivity of the PZT sensor (24.1 mV kPa^{-1}), these results indicate that the pyroelectric contribution to the PZT output was minor under the tested thermal conditions, although it was not entirely absent.

Clinical applicability was further explored by attaching the f-MHE to an arm-mimicking phantom designed to replicate the anatomical structure and mechanical behavior of human soft tissue (Fig. S3 in the ESM) [46,47]. Artificial arterial pressure waveforms within a clinically relevant range (80–120 mmHg) were applied to the phantom, and the corresponding output voltage signals were recorded (Fig. 3(e)). The pressure sensor clearly captured distinct peak features across eight waveform patterns representing systolic and diastolic phases, validating its capability for precise physiological signal detection.

The sensor's response to human-motion-induced mechanical stimuli was also evaluated. Figures 3(f) and 3(g) show output voltage responses to tactile stimuli, including fingertip touching and rubbing, respectively, where the f-MHE was fixed on a flat rigid plate, and the tactile actions were performed using the index finger. In both cases, the pressure sensor reliably captured subtle pressure variations induced by these actions, indicating its capability to detect diverse tactile inputs.

Finally, the wearable applicability of the sensor was demonstrated through biomechanical and physiological motion measurements. When mounted on the index finger, the f-MHE reliably detected finger-bending motions up to 90° and produced consistent signal outputs under repeated bending (Fig. 3(h)). In addition, when attached to the anterior neck, the f-MHE captured reproducible voltage signals associated with swallowing (Fig. 3(i)), confirming its ability to monitor subtle physiological movements. Collectively, these results demonstrate that the piezoelectric pressure sensor integrated in the f-MHE maintains high sensitivity and stable performance under practical loading conditions, supporting its broad applicability for wearable monitoring of human motion and physiological signals.

3.4 Thermoresistive temperature sensor characterization

When the temperature of the conductor changes from a reference temperature T_{ref} to a temperature T, the change in electrical resistance ΔR (= $R - R_{ref}$) can be expressed as Equation (1) [48].

$$\Delta R = R_{ref} \cdot \alpha \cdot \left(T - T_{ref}\right) = R_{ref} \cdot \alpha \cdot \Delta T \quad (1)$$

where R_{ref} and R are the electrical resistances at T_{ref} (25 °C) and T, respectively, and α is the temperature coefficient of resistance (TCR). Based on the resistivity values of Au (2.44×10^{-8} Ω m) and Cr (1.3×10^{-7} Ω m) [49], together with the geometrical parameters of the Au/Cr micropatterns (10 nm-thick Cr and 100 nm-thick Au, 100 μm line width, 100 μm spacing between patterns, and a total pattern length of 700 mm; Fig. 4(a)), R_{ref} and α were calculated to be 1676.9 Ω (Note 1 and Eqs. (S1) and (S2) in the ESM) and 0.0033 $°C^{-1}$ (Note 2 and Eqs. (S3)–(S17) in the ESM), respectively. By substituting these values into

Just Accepted

Equation (1), the designed temperature sensitivity of the sensor ($\Delta R/\Delta T$) was predicted to be 5.53 Ω °C^{-1} (Eq. (S18) in the ESM).

To experimentally characterize the temperature sensor performance, a calibration system was established consisting of a temperature controller, a heating plate, a digital multimeter, and a LabVIEW-based data acquisition system (Fig. 4(b)). The resistance–temperature characteristics were first evaluated during heating and cooling cycles with 1 °C steps over the physiological temperature range of 25–45 °C (Fig. 4(c)). The sensor exhibited a temperature sensitivity of 5.03 Ω °C^{-1}, corresponding to an error of approximately 9% relative to the predicted value (5.53 Ω °C^{-1}) from Equation (1), indicating good agreement between the design prediction and the experimental result. In addition, the sensor showed excellent linearity (R^2 = 0.999) with negligible hysteresis during both heating and cooling cycles.

The temperature resolution was further examined by applying heating and cooling cycles with the temperature precisely controlled at 0.1 °C intervals in the 30–31 °C range (Fig. 4(d)) and the 40–41 °C range (Fig. 4(e)). The sensor maintained highly linear responses and enabled a temperature resolution of <0.1 °C, validating its capability to detect subtle temperature variations.

Because metallic conductors can exhibit piezoresistive behavior under mechanical deformation, the piezoresistive response of the temperature sensor was investigated through two supplementary experiments. Under cyclic bending at constant temperature, the f-MHE experienced a strain variation of approximately 0.16% and generated a PZT peak voltage of approximately 780 mV, whereas the resistance change of the temperature sensor was only 0.432 ± 0.016 Ω, corresponding to an apparent temperature variation of 0.086 ± 0.003 °C (Fig. S4 in the ESM). In a separate fingertip-contact and tapping experiment, strong dynamic mechanical stimulation produced PZT peak voltages of approximately ±700 mV, while the tapping-synchronized resistance fluctuation was only 0.025 Ω, corresponding to an apparent temperature variation of approximately 0.005 °C (Fig. S5 in the ESM). These results indicate that the mechanically induced cross-response of the temperature sensor is minor under the tested conditions, supporting reliable temperature measurement with minimal interference from mechanical deformation. Furthermore, the results support the effectiveness of the serpentine geometry adopted for the temperature sensor in suppressing mechanically induced piezoresistive responses.

Figure 4(f) demonstrates the dynamic temperature sensing capability of the sensor, where heating and cooling cycles between 30 °C and 40 °C were repeated 10 times. The electrical resistance promptly responded to temperature changes, confirming the sensor's fast dynamic response. Notably, the resistance values at 30 °C and 40 °C were highly consistent across repeated cycles, with average values of 1993.55 ± 0.24 Ω at 30 °C and 2043.21 ± 0.29 Ω at 40 °C, demonstrating excellent reproducibility and operational stability.

The measurement stability of the sensor was further evaluated by holding the f-MHE at each temperature set point from 30 to 40 °C for 10 min while continuously recording its resistance output (Fig. 4(g)). At all temperature set points, the resistance remained nearly constant with negligible drift throughout the holding period, confirming stable measurement performance under constant-temperature conditions.

Finally, the applicability of the sensor for detecting human-motion-induced temperature variations was examined by repeatedly touching and detaching the f-MHE, fixed on a rigid plate, using the index finger for seven cycles (Fig. 4(h)). Fingertip contact induced a rapid increase in electrical resistance due to heat transfer to the sensor, whereas fingertip detachment produced a corresponding resistance decrease as the device cooled toward equilibrium. This response pattern was consistently reproduced over repeated contact–detachment cycles.

The temperatures of the rigid plate and fingertip were approximately 25 and 32 °C, respectively. Therefore, fingertip contact and detachment imposed a rapid, step-like change in the thermal boundary condition of the temperature sensor, allowing its response and recovery times to be evaluated from the transient resistance signals shown in Fig. 4(h). The response and recovery times were determined using the 10–90% criterion [50,51]. The response time was defined as the time required for the resistance signal to increase from 10% to 90% of the total resistance change after fingertip contact, whereas the recovery time was defined as the time required for the resistance signal to decrease from 90% to 10% of the total resistance change after fingertip detachment. The five central cycles, corresponding to the second through sixth cycles, were used for the statistical analysis. The resulting response and recovery times were 37.6 ± 3.2 ms and 182.4 ± 9.6 ms, respectively, where the values represent the mean ± standard deviation.

Collectively, these results demonstrate that the f-MHE enables highly reliable, stable, and high-resolution temperature detection under various contact conditions, supporting its suitability for continuous physiological monitoring in dynamic environments.

3.5 Multimodal sensing applications for human motion and physiological monitoring

To evaluate the multimodal sensing capabilities of the f-MHE, the device was tested under representative physiological conditions where both mechanical and thermal stimuli coexist. The experiments were designed to assess the f-MHE's ability to distinguish multiple signals without interference, as well as its sensing stability, reliability, and reproducibility over multiple measurement cycles.

Hand grasping/releasing (Figs. 5(a) and 5(b)): The device was attached to the thumb of a hand wearing an experimental rubber glove, and the grasping and releasing of a metal object were repeated. Upon initiating the grasp, the pressure sensor generated a sharp positive voltage peak (~878 mV) in response to the transient mechanical force change due to the piezoelectric response of the PZT layer. The output then decayed back toward 0 mV as the grasp was maintained, as the applied force became quasi-static, producing minimal additional piezoelectric charge generation. Meanwhile, the temperature sensor exhibited a rapid resistance decrease from 1987 Ω to 1933 Ω upon contact with the cold metal object, followed by saturation as the interface approached thermal equilibrium.

During the release of the object, the pressure sensor produced a sharp negative voltage peak (~−772 mV) corresponding to the rapid unloading of the applied mechanical force and then

Just Accepted

returned to baseline. The temperature sensor showed a corresponding resistance increase due to the cessation of heat transfer to the cold metal object, followed by recovery toward its initial level. The distinct temporal signatures and polarities of the two signals confirm decoupled detection of mechanical and thermal stimuli without electrical interference. Additionally, the consistent responses observed during repeated cycles further demonstrate the stable and reproducible multimodal operation of the device.

Respiration monitoring (Figs. 5(c) and 5(d)): To monitor respiratory activity, the f-MHE was mounted on a face mask. During exhalation, warm exhaled air increased the local pressure inside the mask and induced outward deformation of the mask, generating bending strain in the attached f-MHE. This deformation produced a positive piezoelectric voltage peak of approximately 830 mV. During inhalation, the pressure inside the mask decreased and the mask deformed in the opposite direction, resulting in a negative voltage peak of approximately −679 mV. The relatively high positive and negative PZT voltage outputs originated primarily from bending strain induced by the cyclic deformation of the face mask, rather than from direct airflow pressure or the pyroelectric response of the PZT film (Figs. S6 and S7 in the ESM).

Simultaneously, the temperature sensor tracked thermal changes induced by the respiratory airflow. The sensor's resistance increased during exhalation due to warm air exposure and decreased during inhalation due to cooler ambient air. The stable and repeatable waveforms observed across multiple breathing cycles indicate robust performance under dynamic conditions. Moreover, the periodic patterns of pressure and temperature signals clearly reflected changes in respiratory rhythm and frequency, demonstrating the f-MHE's ability to monitor both the mechanical (pressure) and thermal (temperature) aspects of respiration. This highlights its potential for continuous respiration monitoring and pulmonary health assessment.

Exercise-induced physiological changes (Figs. 5(e)–5(i): The wearable applicability of the f-MHE was further examined by attaching the device to the wrist to simultaneously measure arterial pulse (pressure) and skin temperature across three different states: pre-exercise, immediately post-exercise (immediately after 30 min of running), and post-exercise recovery (10 min after completion of the excise). During the pre-exercise state, the pressure sensor captured stable, periodic pulse waveforms with clearly distinguishable systolic and diastolic peaks, indicating a steady cardiovascular condition at rest. Concurrently, the temperature sensor maintained a nearly constant baseline resistance, indicating a stable skin-device interface under minimal metabolic heat generation and steady cutaneous perfusion.

In the immediately post-exercise state, both the pressure and temperature sensors exhibited pronounced physiological responses. The pressure signal showed increased pulse frequency (shorter peak intervals) and elevated peak-to-peak amplitude, reflecting the effects of exercise-induced sympathetic activation that increases heart rate and myocardial contractility, resulting in enhanced stroke volume and arterial pulse pressure. Simultaneously, the temperature sensor displayed a gradual increase in resistance, consistent with the rise in skin temperature due to increased metabolic heat production and thermoregulatory adjustments (e.g., cutaneous vasodilation), which increase skin blood perfusion.

During the post-exercise recovery state, both pressure and temperature signals gradually returned toward their pre-exercise profiles. The pulse waveform decreased in frequency and amplitude, reflecting the restoration of autonomic balance (reduced sympathetic drive and parasympathetic reactivation). Similarly, the temperature-related resistance trend approached baseline as heat production decreased and thermal homeostasis was re-established.

Quantitative assessment: Quantitative assessment of exercise-induced physiological changes was conducted using four indicators: main peak interval, peak-to-peak voltage, augmentation index, and average resistance. These indicators were extracted from the pulse wave and skin-temperature signals measured by the f-MHE (Fig. 5(e)) and compared across the three conditions (pre-exercise, immediately post-exercise, and recovery). As shown in Fig. 5(f), the main peak interval decreased from 77.68 ms before exercise to 55.59 ms immediately after exercise and partially recovered to 65.01 ms during recovery, indicating an increased heart rate following physical exertion. This is consistent with sympathetic activation during exercise and parasympathetic reactivation during recovery.

Figure 5(g) shows that the peak-to-peak voltage amplitude increased from 85.08 mV at rest to 109.91 mV after exercise and decreased to 86.06 mV during recovery. The post-exercise increase reflects heightened systolic ejection and elevated pulse pressure, while the recovery trend signifies normalization of cardiac output and vascular tone. Figure 5(h) presents the augmentation index, which decreased from 54.63% before exercise to 45.70% immediately after exercise and then recovered to 49.45% during recovery. This reduction is mainly attributed to enhanced systolic peak after exercise, leading to a lower contribution from the reflected wave.

Figure 5(i) shows that the average resistance measured by the temperature sensor increased from 1.983 kΩ before exercise to 2.010 kΩ immediately post-exercise and then slightly decreased to 1.988 kΩ during recovery. These changes correlate with skin-temperature elevation due to metabolic heat generation and increased cutaneous perfusion during exercise, followed by gradual cooling as thermoregulatory processes restore heat balance.

Collectively, these results demonstrate the f-MHE's ability to reliably and reproducibly capture dynamic physiological variations across multiple modalities, while consistently providing effectively decoupled pressure and temperature signals. These findings validate the device's potential as a wearable electronic platform for continuous health monitoring.

4 Conclusions

In this study, we developed a monolithically integrated f-MHE platform based on a perovskite PZT piezoelectric thin film for the simultaneous monitoring of pressure and temperature signals associated with human motion and physiological activity, with negligible cross-sensitivity between the two sensing channels. By implementing a single-layer monolithic design in which both sensing elements are patterned within a unified thin-film architecture, the platform eliminates multilayer stacking

Just Accepted

and repeated alignment/etching steps, thereby reducing mechanically vulnerable interfacial boundaries, improving fabrication efficiency and manufacturing yield, and enhancing mechanical integrity under deformation. Consequently, the device achieves an ultrathin (<5 μm), mechanically compliant form factor that conformally attaches to curved and deformable surfaces, including human skin, enabling stable signal acquisition during wearable operation. The integrated device demonstrated high-performance sensing characteristics: the piezoelectric pressure sensor exhibited a sensitivity of 24.1 mV kPa^{-1} with a pressure resolution of <0.1 kPa over 0.1–25 kPa and robust durability under cyclic loading (100,000 cycles), while the thermoresistive temperature sensor showed a sensitivity of 5.03 Ω $°C^{-1}$ with a temperature resolution of <0.1 °C over the physiological range of 25–45 °C, featuring high linearity and negligible hysteresis. Importantly, the multimodal capability of the f-MHE was validated through real-time, stable, and reproducible monitoring of representative physiological and behavioral signals—including hand grasping/releasing, respiration, and exercise-induced changes in arterial pulse and skin temperature—while maintaining independent operation without electrical interference between the two sensing modalities. Overall, this work establishes a structurally simple yet efficient and reliable approach to multifunctional sensor integration using monolithic thin-film design, and the demonstrated combination of ultrathin conformability, mechanical robustness, and low-crosstalk multimodal sensing supports the strong potential of the f-MHE as a next-generation wearable electronic platform for continuous health monitoring.

Electronic Supplementary Material: Supplementary Material (photograph of the laser lift-off process, pyroelectric response of the PZT pressure sensor, cross-sectional schematic of the arm phantom replicating the anatomical layers of human tissue, piezoresistive responses of the thermoresistive temperature sensor, airflow-induced responses of the f-MHE, bending-induced piezoelectric response of the f-MHE, and theoretical calculation of R_{ref} and α used in Eq. (1)) is available in the online version of this article at https://doi.org/10.26599/NR.2026.94909204.

Data availability

All data needed to support the conclusions in this paper are presented in the manuscript and the Electronic Supplementary Material. Additional data related to this paper may be requested from the corresponding author upon reasonable request.

Acknowledgements

This work was supported by the Quantum Scopes for Quantum Materials Property Evaluation funded by the Korea Research Institute of Standards and Science (KRISS-2026-KP2026-0004), the National Research Council of Science and Technology (NST) grant funded by the Korean government (MSIT) (No. CRC23021-000), and the HSMU Research Grant (2025).

Declaration of competing interest

All the contributing authors report no conflict of interests in this work.

Author contribution statement

M. K.: Conceptualization, methodology, investigation, formal analysis, data curation, visualization, and writing—original draft. K. L.: Methodology, investigation, and validation. M. S. K.: Investigation and validation. I. D.: Methodology, resources, and validation. S.-G. H.: Conceptualization, supervision, project administration, funding acquisition, and writing—review and editing. All the authors have approved the final manuscript.

Informed consent

Written informed consent for participation was obtained from the participant prior to the experiments.

Ethics statement

All experiments involving a human participant were conducted in accordance with a protocol approved by the Public Institutional Review Board designated by the Ministry of Health and Welfare of the Republic of Korea (IRB No. 2026-2055-001).

Use of AI statement

During the preparation of this work, the authors used ChatGPT (OpenAI) to assist with English-language editing, reference formatting, and refinement of manuscript wording. The authors reviewed and edited the AI-assisted content as needed and take full responsibility for the content of the publication.

References

[1] Trung, T. Q.; Lee, N.-E. Flexible and stretchable physical sensor integrated platforms for wearable human-activity monitoring and personal healthcare. *Adv. Mater.* **2016**, 28, 4338–4372.

[2] Jin, H.; Abu-Raya, Y. S.; Haick, H. Advanced materials for health monitoring with skin-based wearable devices. *Adv. Healthc. Mater.* **2017**, 6, 1700024.

[3] Liu, K. et al. Advances in flexible organic field-effect transistors and their applications for flexible electronics. *npj Flex. Electron.* **2022**, 6, 1.

[4] Wang, X.; Liu, Z.; Zhang, T. Flexible sensing electronics for wearable/attachable health monitoring. *Small* **2017**, 13, 1602790.

[5] Muthu, B. et al. IoT based wearable sensor for diseases prediction and symptom analysis in healthcare sector. *Peer-to-Peer Netw. Appl.* **2020**, 13, 2123–2134.

[6] Kakria, P.; Tripathi, N. K.; Kitipawang, P. A real-time health monitoring system for remote cardiac patients using smartphone and wearable sensors. *Int. J. Telemed. Appl.* **2015**, 2015, 373474.

[7] Lim, H.-R. et al. Advanced soft materials, sensor integrations, and applications of wearable flexible hybrid electronics in healthcare, energy, and environment. *Adv. Mater.* **2020**, 32, 1901924.

[8] Al-Makhadmeh, Z.; Tolba, A. Utilizing IoT wearable medical device for heart disease prediction using higher order Boltzmann model: A classification approach. *Measurement* **2019**, 147, 106815.

[9] Weiss, G. M.; Yoneda, K.; Hayajneh, T. Smartphone and smartwatch-based biometrics using activities of daily living. *IEEE Access* **2019**, 7, 133190–133202.

[10] Kheirkhahan, M. et al. A smartwatch-based framework for real-time and online assessment and mobility monitoring. *J. Biomed. Inform.* **2019**, 89, 29–40.

[11] Strik, M. et al. The use of smartwatch electrocardiogram beyond arrhythmia detection. *Trends Cardiovasc. Med.* **2024**, 34, 174–180.

[12] Martis, R. J.; Acharya, U. R.; Adeli, H. Current methods in electrocardiogram characterization. *Comput. Biol. Med.* **2014**, 48, 133–149.

[13] Sörnmo, L.; Laguna, P. Electrocardiogram (ECG) signal processing. *Wiley Encycl. Biomed. Eng.* **2006**, 1–16.

Just Accepted

[14] Kumar, J. S.; Bhuvaneswari, P. Analysis of electroencephalography (EEG) signals and its categorization–a study. *Procedia Eng.* **2012**, 38, 2525–2536.

[15] Pang, C. et al. A flexible and highly sensitive strain-gauge sensor using reversible interlocking of nanofibres. *Nat. Mater.* **2012**, 11, 795–801.

[16] Schwartz, G. et al. Flexible polymer transistors with high pressure sensitivity for application in electronic skin and health monitoring. *Nat. Commun.* **2013**, 4, 1859.

[17] Choong, C.-L. et al. Highly stretchable resistive pressure sensors using a conductive elastomeric composite on a micropyramid array. *Adv. Mater.* **2014**, 26, 3451–3458.

[18] Luo, N. et al. Flexible piezoresistive sensor patch enabling ultralow power cuffless blood pressure measurement. *Adv. Funct. Mater.* **2016**, 26, 1178–1187.

[19] Boutry, C. M. et al. Biodegradable and flexible arterial-pulse sensor for the wireless monitoring of blood flow. *Nat. Biomed. Eng.* **2019**, 3, 47–57.

[20] Dagdeviren, C. et al. Conformable amplified lead zirconate titanate sensors with enhanced piezoelectric response for cutaneous pressure monitoring. *Nat. Commun.* **2014**, 5, 4496.

[21] Kim, M. et al. Flexible piezoelectric pressure sensors fabricated from nanocomposites with enhanced dispersion and vapor permeability for precision pulse wave monitoring. *ACS Appl. Nano Mater.* **2023**, 6, 22025–22035.

[22] Park, D. Y. et al. Self-powered real-time arterial pulse monitoring using ultrathin epidermal piezoelectric sensors. *Adv. Mater.* **2017**, 29, 1702308.

[23] Wang, H. S. et al. Biomimetic and flexible piezoelectric mobile acoustic sensors with multiresonant ultrathin structures for machine learning biometrics. *Sci. Adv.* **2021**, 7, eabe5683.

[24] Ha, M. et al. Skin-inspired hierarchical polymer architectures with gradient stiffness for spacer-free, ultrathin, and highly sensitive triboelectric sensors. *ACS Nano* **2018**, 12, 3964–3974.

[25] Zhang, S. et al. On-skin ultrathin and stretchable multifunctional sensor for smart healthcare wearables. *npj Flex. Electron.* **2022**, 6, 11.

[26] Nakata, S. et al. Wearable, flexible, and multifunctional healthcare device with an integrated ISFET chemical sensor for simultaneous sweat pH and skin temperature monitoring. *ACS Sens.* **2017**, 2, 443–448.

[27] Yamamoto, Y. et al. Printed multifunctional flexible device with an integrated motion sensor for health care monitoring. *Sci. Adv.* **2016**, 2, e1601473.

[28] Hozumi, S. et al. Multimodal wearable sensor sheet for health-related chemical and physical monitoring. *ACS Sens.* **2021**, 6, 1918–1924.

[29] Liu, H. et al. A flexible multimodal sensor that detects strain, humidity, temperature, and pressure with carbon black and reduced graphene oxide hierarchical composite on paper. *ACS Appl. Mater. Interfaces* **2019**, 11, 40613–40619.

[30] Alam, M. M. et al. Ultra-flexible nanofiber-based multifunctional motion sensor. *Nano Energy* **2020**, 72, 104672.

[31] Yin, F. et al. A waterproof and breathable cotton/rGO/CNT composite for constructing a layer-by-layer structured multifunctional flexible sensor. *Nano Res.* **2022**, 15, 9341–9351.

[32] Hua, Q. et al. Skin-inspired highly stretchable and conformable matrix networks for multifunctional sensing. *Nat. Commun.* **2018**, 9, 244.

[33] Kim, M. et al. Piezoelectric nanocomposite-based multifunctional wearable bioelectronics for mental stress analysis utilizing physiological signals. *Adv. Mater. Technol.* **2024**, 9, 2301610.

[34] Narute, P. et al. Electrical contact design for stable and reliable measurement of electromechanical properties in graphene on flexible substrates. *Mater. Des.* **2025**, 256, 114293.

[35] Park, K.-I. et al. Highly-efficient, flexible piezoelectric PZT thin film nanogenerator on plastic substrates. *Adv. Mater.* **2014**, 26, 2514–2520.

[36] Bian, J. et al. Theoretical and experimental studies of laser lift-off of nonwrinkled ultrathin polyimide film for flexible electronics. *Appl. Surf. Sci.* **2020**, 499, 143910.

[37] Dutta, M. et al. Optical and microstructural characterization of multilayer Pb(Zr0.52Ti0.48)O3 thin films correlating ellipsometry and nanoscopy. *J. Mater. Sci.* **2016**, 51, 7944–7955.

[38] Chirila, C. F. et al. Controlling polarization direction in epitaxial Pb(Zr0.2Ti0.8)O3 films through Nb (n-type) and Fe (p-type) doping. *Sci. Rep.* **2022**, 12, 755.

[39] Rouquette, J. et al. Use of resonance Raman spectroscopy to study the phase diagram of PbZr0.52Ti0.48O3. *Phys. Rev. B* **2006**, 73, 224118.

[40] Beklešovas, B. et al. Structural, morphologic, and ferroelectric properties of PZT films deposited through layer-by-layer reactive DC magnetron sputtering. *Coatings* **2022**, 12, 717.

[41] Fernandez-Osorio, A. L. et al. Preparation of free-standing Pb(Zr0.52Ti0.48)O3 nanoparticles by sol–gel method. *J. Sol-Gel Sci. Technol.* **2007**, 42, 145–149.

[42] Qi, H. et al. Ferroelectric properties of the flexible Pb(Zr0.52Ti0.48)O3 thin film on mica. *J. Mater. Sci.: Mater. Electron.* **2020**, 31, 3042–3047.

[43] Doh, I.; Lim, H. K.; Ahn, B. Calibration of oscillometric non-invasive devices for monitoring blood pressure. *Metrologia* **2015**, 52, 291–296.

[44] Kesim, M. T.; Zhang, J.; Trolier-McKinstry, S.; Mantese, J. V.; Whatmore, R. W.; Alpay, S. P. Pyroelectric response of lead zirconate titanate thin films on silicon: Effect of thermal stresses. *J. Appl. Phys.* **2013**, 114, 204101.

[45] Wang, B.; Chan, H. L. W.; Kwok, K. W.; Ploss, B.; Choy, C. L.; Tong, K. Y. Effect of fatigue on the pyroelectric and dielectric properties of PZT films. *J. Eur. Ceram. Soc.* **2001**, 21, 1589–1592.

[46] Lee, B. et al. Correlation analysis of human upper arm parameters to oscillometric signal in automatic blood pressure measurement. *Sci. Rep.* **2022**, 12, 19763.

[47] Min, S. et al. Clinical validation of a wearable piezoelectric blood-pressure sensor for continuous health monitoring. *Adv. Mater.* **2023**, 35, 2301627.

[48] Scorzoni, A.; Baroncini, M.; Placidi, P. On the relationship between the temperature coefficient of resistance and the thermal conductance of integrated metal resistors. *Sens. Actuators A Phys.* **2004**, 116, 137–144.

[49] Leonard, W. F.; Ramey, R. L. Temperature coefficient of resistance in thin metal films. *J. Appl. Phys.* **1966**, 37, 3634–3635.

[50] Trung, T. Q.; Ramasundaram, S.; Hwang, B.-U.; Lee, N.-E. An all-elastomeric transparent and stretchable temperature sensor for body-attachable wearable electronics. *Adv. Mater.* **2016**, 28, 502–509.

[51] Yokota, T.; Inoue, Y.; Terakawa, Y.; Reeder, J.; Kaltenbrunner, M. et al. Ultraflexible, large-area, physiological temperature sensors for multipoint measurements. *Proc. Natl. Acad. Sci. U.S.A.* **2015**, 112, 14533–14538.

Just Accepted

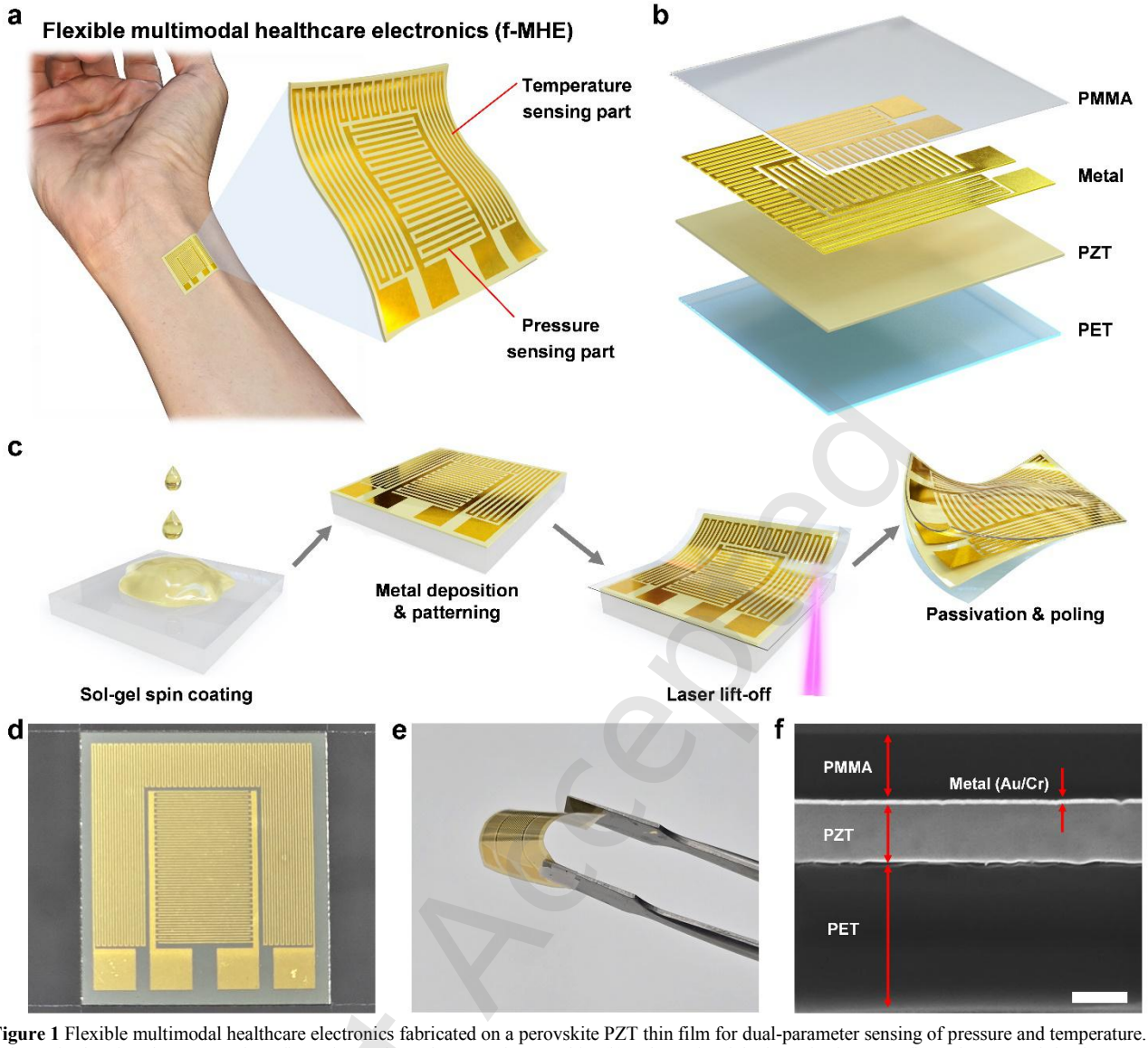


Figure 1 Flexible multimodal healthcare electronics fabricated on a perovskite PZT thin film for dual-parameter sensing of pressure and temperature. (a) Schematic showing the structural configuration and attachment to human skin. (b) Schematic of the layer-by-layer configuration. (c) Fabrication process. (d) Photograph taken from the top (18 mm × 16 mm sensing area). (e) Photograph of the bent device demonstrating its high flexibility. (f) Cross-sectional SEM image (scale bar: 1 μm).

Just Accepted

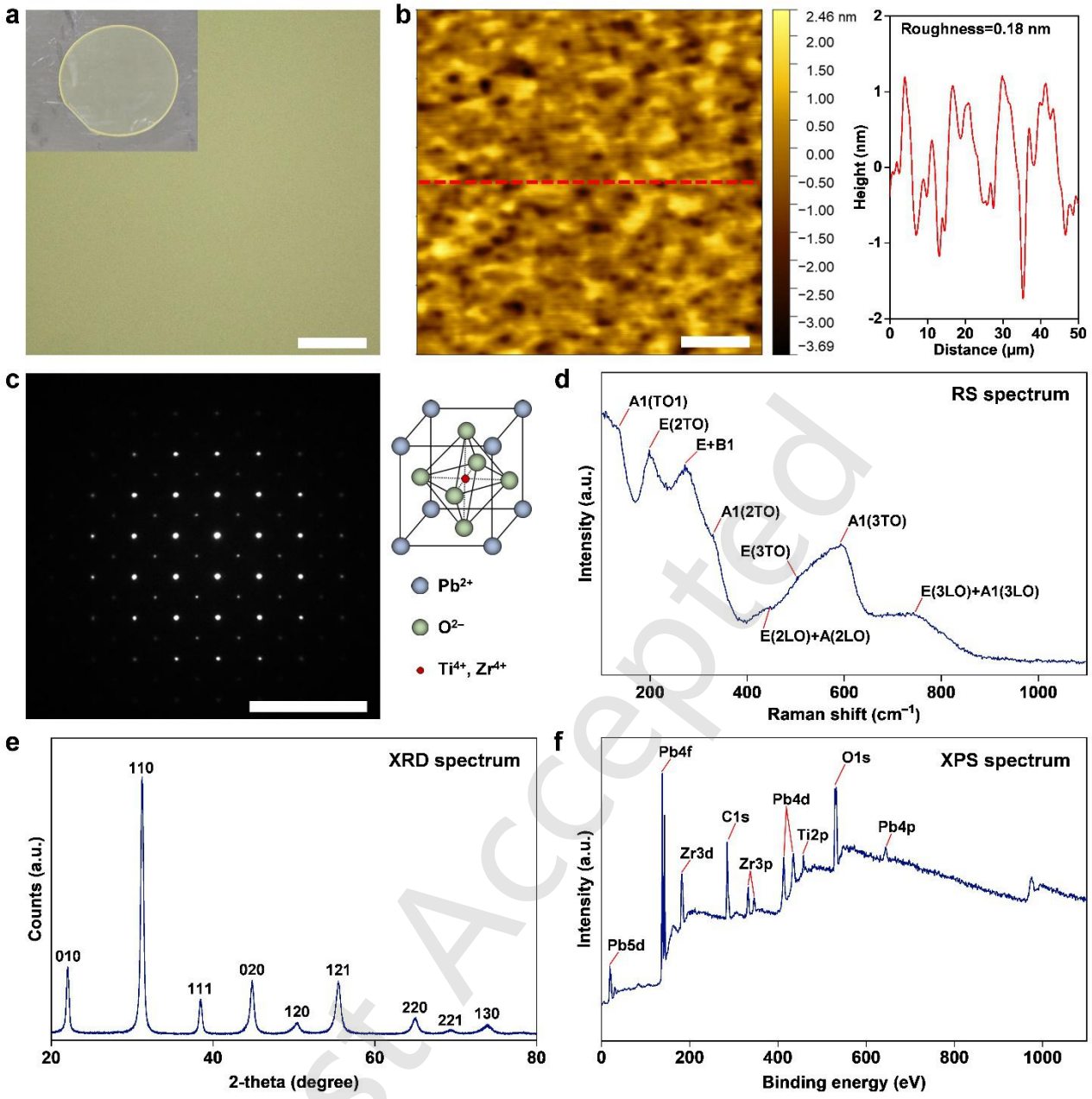


Figure 2 Morphological, structural, and chemical properties of the fabricated PZT thin film. (a) Bright-field optical image of the surface (scale bar: 10 μm). The inset shows a photograph of the PZT film fabricated on a 2-inch sapphire wafer. (b) AFM topographic image of the surface (scale bar: 10 μm) and height profile along the red dashed line in the left panel. (c) TEM SAED pattern of the PZT film (scale bar: 10 1/nm) and the corresponding crystalline lattice structure of perovskite PZT. (d) Raman spectrum of the PZT film. (e) XRD spectrum of the PZT film. (f) XPS spectrum of the PZT film.

Just Accepted

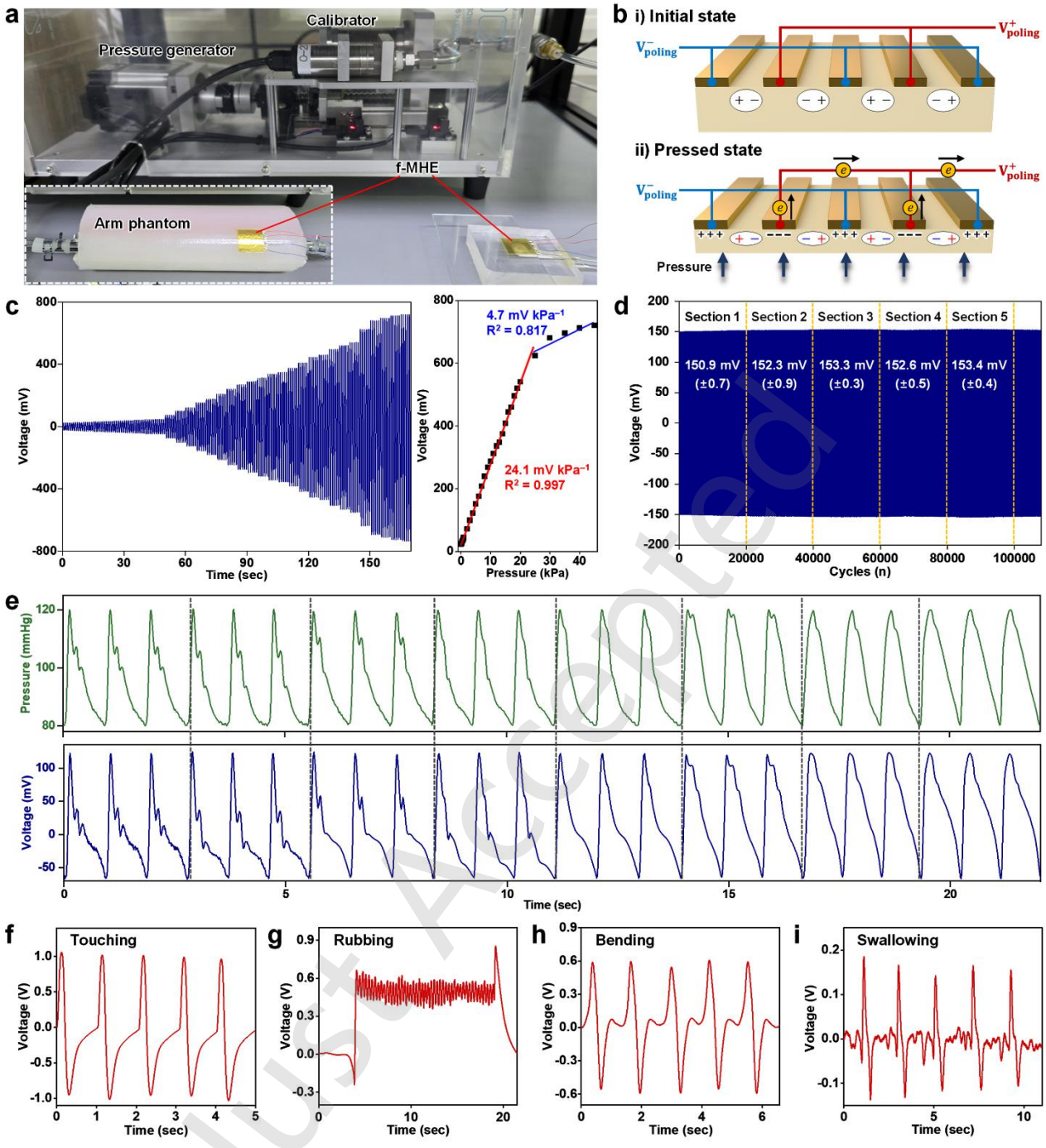


Figure 3 Piezoelectric pressure sensor properties of the f-MHE and its applications for detecting physiological signals and human motions. (a) Experimental setup for characterizing the pressure sensor performance using a custom-built pressure simulator. (b) Schematic illustrating the mechanism of piezoelectricity in the pressure sensor. (c) Output voltage responses of the pressure sensor under periodically varying pressures from 0 to 45 kPa. (d) Long-term stability test under cyclic pressure loading of 5 kPa at 5 Hz for 100,000 cycles. (e) Simulated arterial pressure waveform (80–120 mmHg) and corresponding voltage output obtained from the f-MHE attached to an arm phantom. Output voltage signals obtained from the f-MHE under (f) fingertip touching, (g) finger rubbing, (h) finger bending, and (i) swallowing motion.

Just Accepted

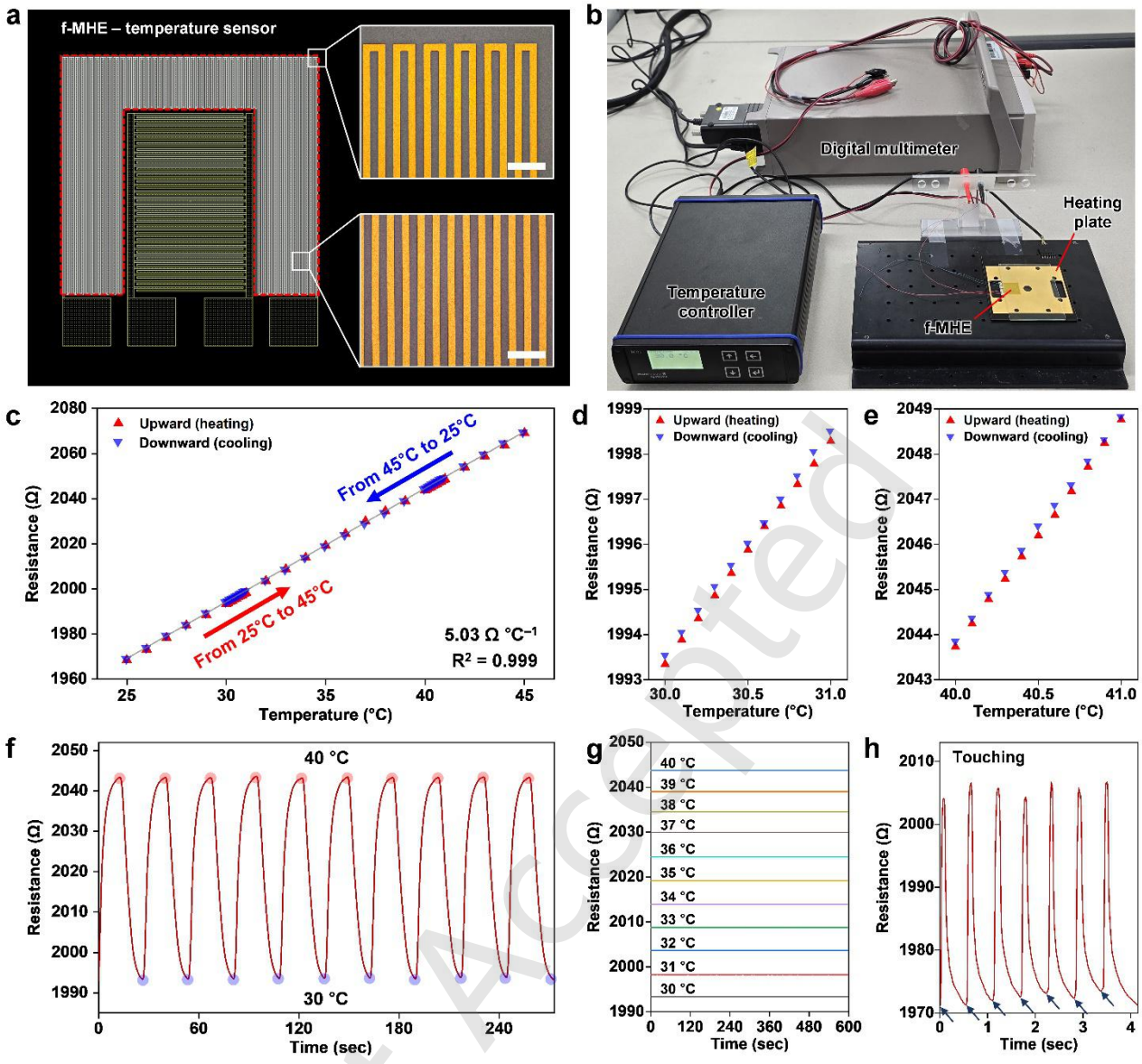


Figure 4 Thermoresistive temperature sensor properties of the f-MHE and its application for detecting human-motion-induced temperature stimulus. (a) Overall mask layout of the f-MHE and optical images of the micropatterned Au/Cr serpentine structure (scale bar: 500 μm). (b) Photograph showing the experimental setup for characterizing the temperature sensor performance. (c) Electrical resistance–temperature curves during heating and cooling with 1 °C intervals from 25 to 45 °C. Electrical resistance–temperature curves during heating and cooling with 0.1 °C intervals at (d) 30–31 °C and (e) 40–41 °C. (f) Dynamic temperature sensing performance under repeated heating and cooling cycles between 30 °C and 40 °C. (g) Measurement stability test at 30–40 °C, with the temperature maintained constant for 10 minutes at each temperature. (h) Electrical resistance responses under repeated fingertip touching of the f-MHE.

Just Accepted

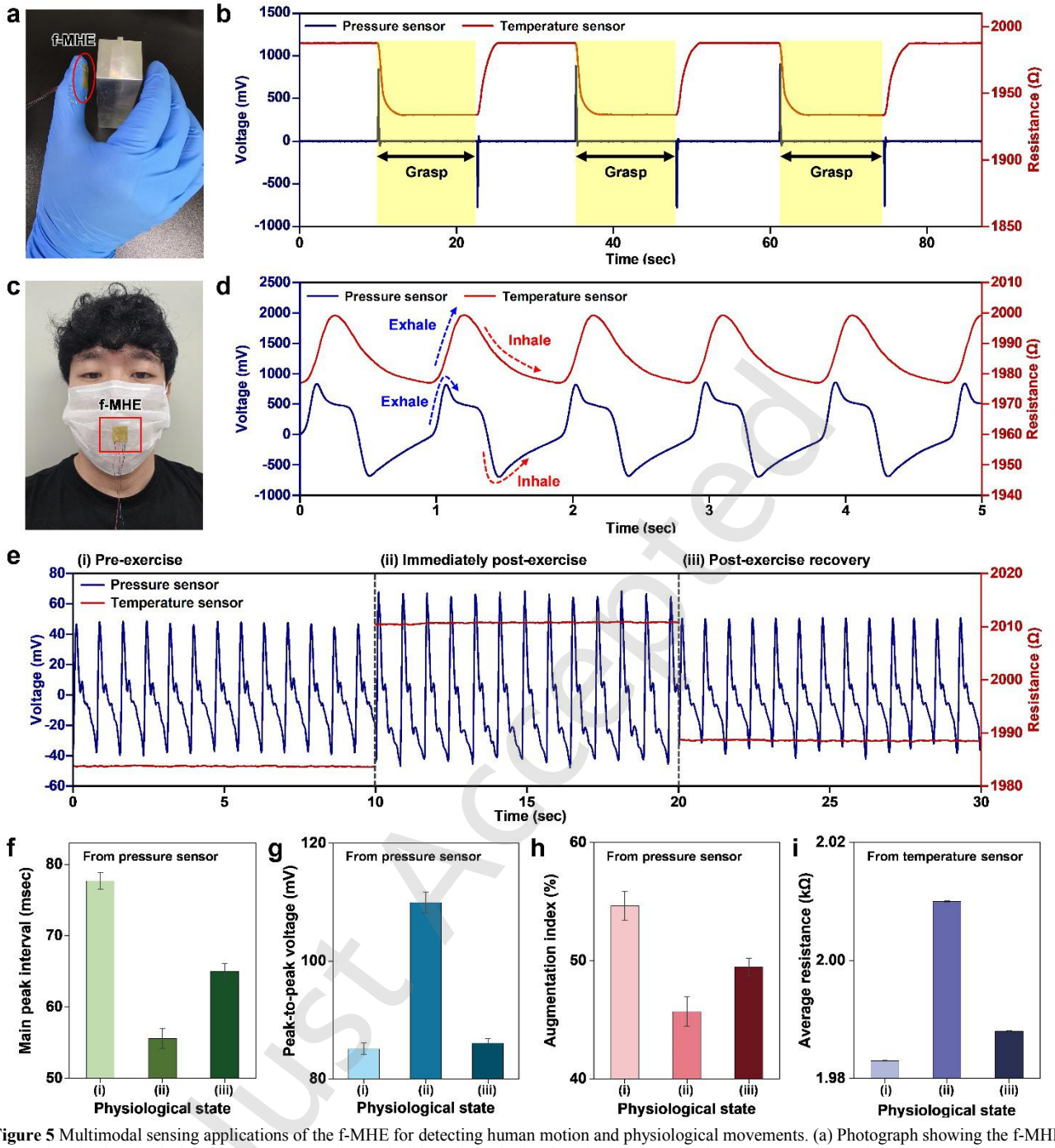


Figure 5 Multimodal sensing applications of the f-MHE for detecting human motion and physiological movements. (a) Photograph showing the f-MHE attached to the thumb of a hand wearing an experimental rubber glove, during the gripping and releasing of a metal object. (b) Pressure and temperature sensor signal outputs obtained from the repeated gripping and releasing of the metal object, as shown in (a). (c) Photograph showing the f-MHE mounted on a face mask for respiration monitoring. (d) Pressure and temperature sensor signal outputs obtained from repeated respiration motions, as shown in (c). (e) Wearable application for monitoring arterial pulse and skin temperature to assess exercise-induced physiological changes, with the f-MHE attached to the wrist. (f) Main peak interval (arterial pulse), (g) peak-to-peak voltage (arterial pulse), (h) augmentation index (arterial pulse), and (i) average electrical resistance (skin temperature) analyzed from the arterial pulse and skin temperature signals shown in (e) at three different physiological conditions .

Just Accepted

Electronic Supplementary Material

Monolithically integrated flexible multimodal healthcare electronics on perovskite piezoelectric thin film for human motion and physiological signal monitoring

Mookyum Kim[1], Kangsan Lee[2,3], Myeong Seok Ko[2,3], Il Doh[2,4], and Seong-Gu Hong[2,3,5]

[1] *Department of Bio-Healthcare, Hwasung Medi-Science University, Gyeonggi-do 18274, Republic of Korea*
[2] *Department of Precision Measurement Engineering, University of Science and Technology, Daejeon 34113, Republic of Korea*
[3] *Convergence Research Center for Meta-Touch, Korea Research Institute of Standards and Science, Daejeon 34113, Republic of Korea*
[4] *Division of Biomedical Metrology, Korea Research Institute of Standards and Science, Daejeon 34113, Republic of Korea*
[5] *Division of Chemical and Material Metrology, Korea Research Institute of Standards and Science, Daejeon 34113, Republic of Korea*

Address correspondence to sghong@kriss.re.kr

Supporting information to https://doi.org/10.26599/NR.2026.94909204

Just Accepted

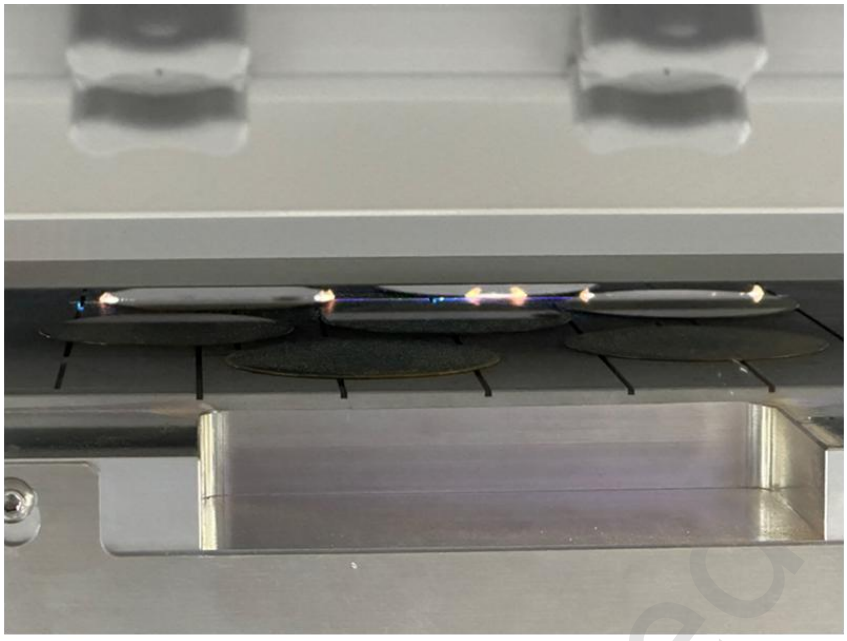


Figure S1 Photograph of the laser lift-off process, where 308 nm XeCl excimer laser irradiation induces interfacial separation of the PZT film from the sapphire substrate.

Just Accepted

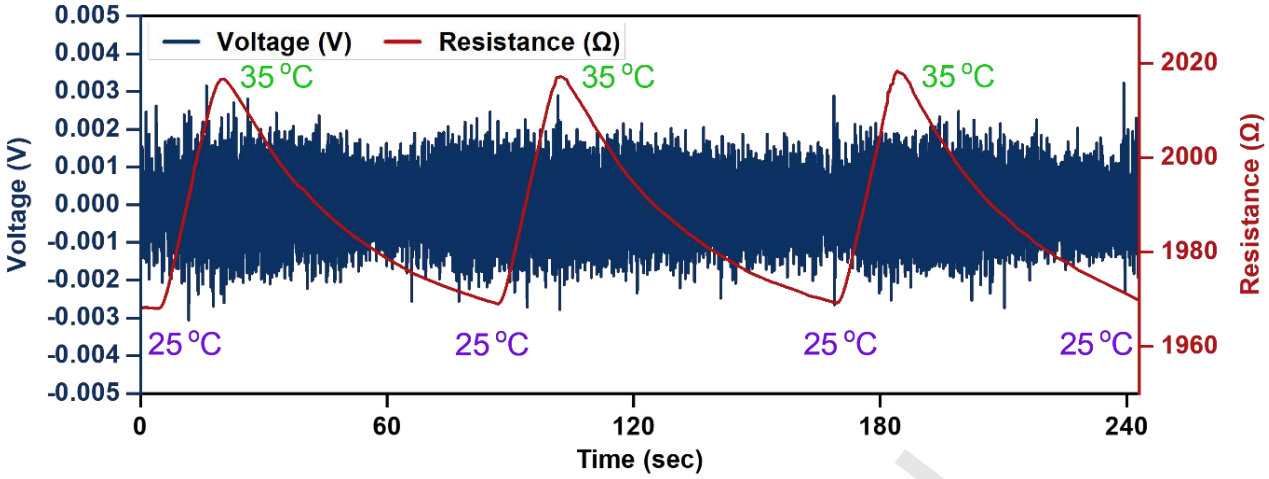


Figure S2 Pyroelectric response of the PZT pressure sensor in the f-MHE. The f-MHE was placed on a heating plate without externally applied mechanical deformation and subjected to three heating and cooling cycles between 25 and 35 °C. During the thermal cycles, the maximum voltage output of the PZT sensor was approximately 3 mV and showed no systematic dependence on temperature. These results indicate that the pyroelectric response of the PZT sensor makes only a negligible contribution to its voltage output under the tested temperature conditions.

Just Accepted

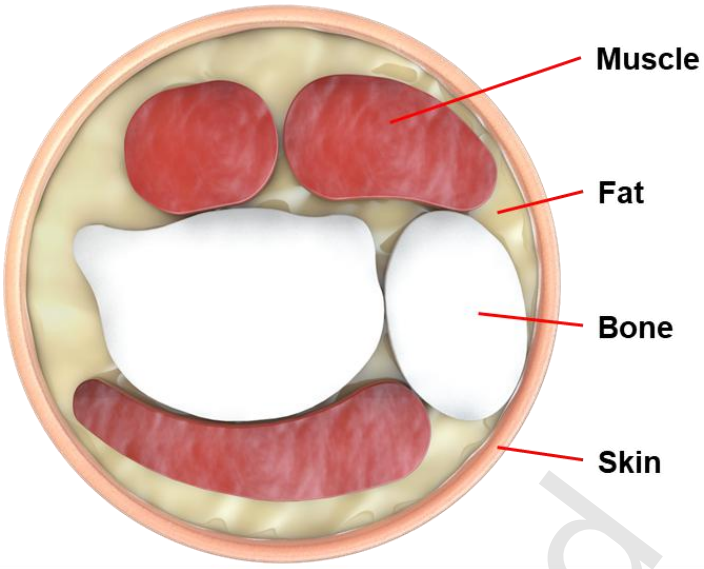


Figure S3 Cross-sectional schematic of the arm phantom replicating the anatomical layers of human tissue (skin, fat, muscle, and bone), used to evaluate the pressure sensing performance of the f-MHE.

Just Accepted

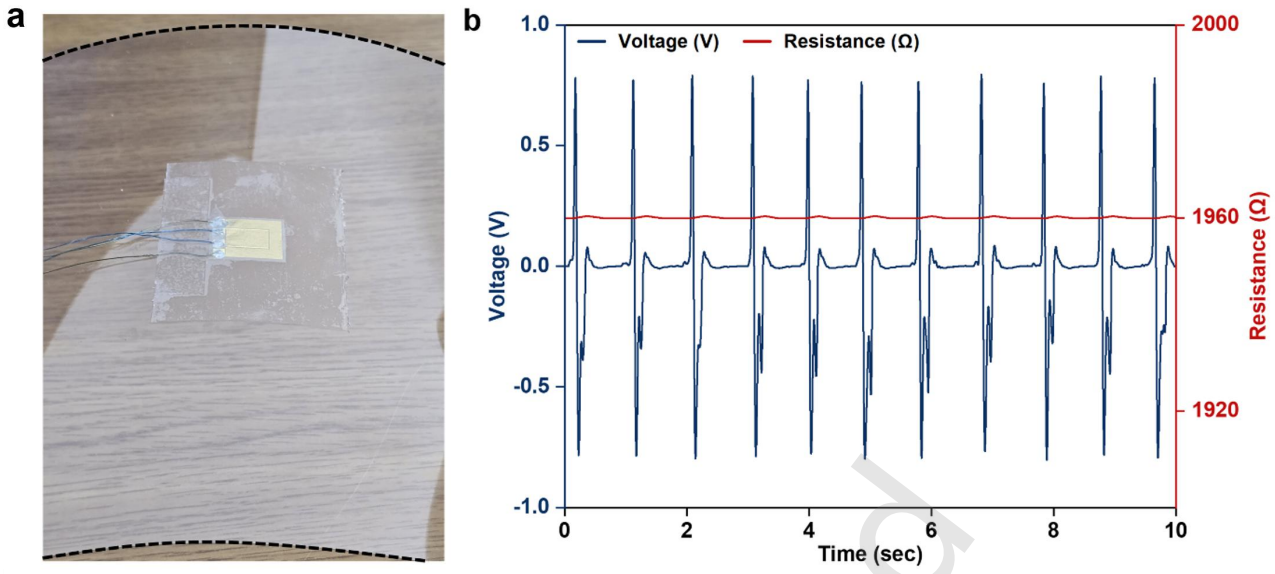


Figure S4 Piezoresistive response of the thermoresistive temperature sensor in the f-MHE under cyclic mechanical bending at constant temperature. (a) Photograph of the experimental setup. (b) PZT output-voltage and temperature-sensor resistance responses during 11 bending and release cycles.

The f-MHE was attached to the center of a 400 μm-thick PET sheet measuring 30 cm in length and 20 cm in width. One end of the PET sheet was fixed, while the other end was displaced inward to induce repeated bending and release under constant-temperature conditions (Figure S4a). The PET sheet was initially pre-bent to an end-to-end distance of 28 cm, corresponding to a central deflection of 3.1 cm, a radius of curvature of approximately 33.2 cm, and a surface bending strain of 0.06%. It was then bent further to an end-to-end distance of 18 cm, corresponding to a central deflection of 9.1 cm, a radius of curvature of approximately 9.0 cm, and a surface bending strain of 0.22%. The sheet was subsequently returned to its initial pre-bent state with an end-to-end distance of 28 cm. Thus, the f-MHE experienced a cyclic strain variation of approximately 0.16% during each bending and release cycle. This procedure was repeated 11 times.

As shown in Figure S4b, the PZT pressure sensor generated peak voltages of approximately 780 mV during the bending and release cycles, confirming that substantial dynamic mechanical deformation was transferred to the f-MHE. Nevertheless, the resistance difference measured between the two deformation states was only 0.432 ± 0.016 Ω over the 11 cycles, where the values represent the mean ± standard deviation. Based on the temperature sensitivity of 5.03 Ω $°C^{-1}$, this resistance variation corresponds to an apparent temperature change of only 0.086 ± 0.003 °C. These results demonstrate that the mechanically induced resistance variation of the temperature sensor is minor under the tested bending conditions.

The bending-strain calculation:

The bent profile of the PET film was approximated as a circular arc. The neutral axis was assumed to lie at the mid-plane of the 400 μm-thick PET film. Because the f-MHE was attached to the outer surface of the PET film, the distance from the neutral axis to the sensor was approximated as 200 μm, with the thickness of the f-MHE neglected relative to that of the PET film.

The radius of curvature (R), and the surface bending strain (ε), were calculated using Equations (A) and (B), respectively [1,2]:

$$R = \frac{c^2}{8h} + \frac{h}{2} \quad \text{(A)}$$

$$\varepsilon = \frac{y}{R} \quad \text{(B)}$$

where c is the end-to-end distance of the bent PET film, h is the central deflection, and y = 200 μm is the distance from the neutral axis of the PET film to the sensor.

[1] Pathak, A.; Deshpande, V. S.; McMeeking, R. M.; Evans, A. G. The simulation of stress fibre and focal adhesion development in cells on patterned substrates. *J. R. Soc. Interface* **2008**, 5, 507–524.

[2] Hwang, B.; Lim, S.; Park, M.; Han, S. M. Neutral plane control by using polymer/graphene flake composites for flexible displays. *RSC Adv.* **2017**, 7, 8186–8191.

Just Accepted

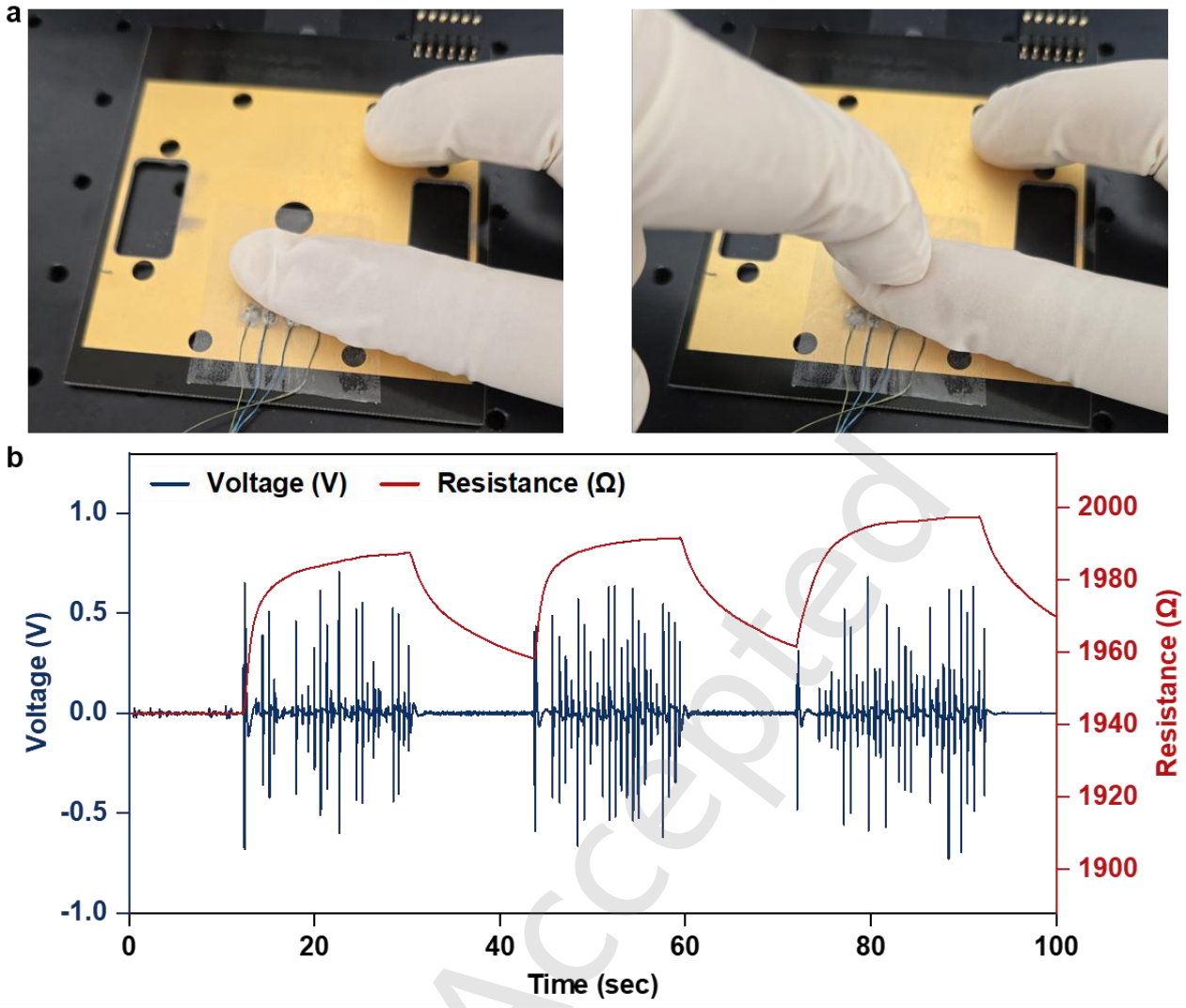


Figure S5 Piezoresistive response of the temperature sensor in the f-MHE during repeated fingertip contact and tapping. (a) Photograph of the experimental setup. (b) PZT output-voltage and temperature-sensor resistance responses during three fingertip contact-and-tapping cycles.

The f-MHE was attached to a metal plate maintained at 20 °C. A latex-gloved index finger was placed in contact with the f-MHE, and repeated tapping was subsequently applied to the dorsal surface of the contacting finger using another latex-gloved index finger (Figure S5a). The finger-contact and tapping sequence was repeated three times. As shown in Figure S5b, the PZT pressure sensor generated positive and negative peak voltages of +0.7 and −0.7 V, respectively, confirming the application of strong dynamic mechanical stimuli. Meanwhile, the resistance of the temperature sensor exhibited the gradual change expected from heat transfer between the warmer finger and the cooler f-MHE, without a discernible resistance response synchronized with the tapping events. The average peak-to-valley resistance fluctuation associated with tapping was only 0.025 Ω, corresponding to an apparent temperature variation of approximately 0.005 °C. These results indicate that the applied tapping stimuli had no meaningful influence on the temperature measurement under the tested conditions.

Just Accepted

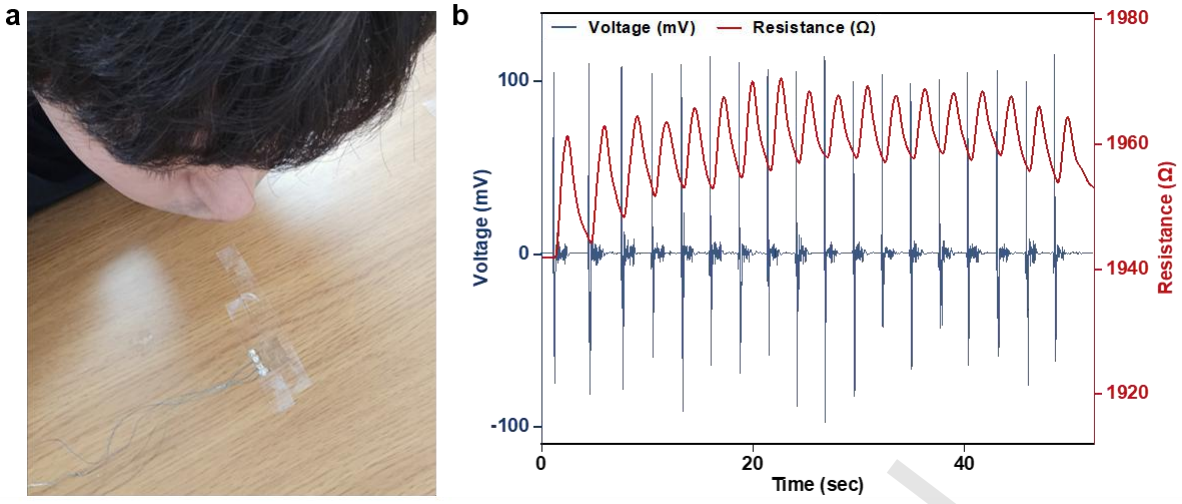


Figure S6 Airflow-induced responses of the f-MHE fixed to a rigid substrate to suppress macroscopic bending during repeated strong exhalation. (a) Photograph of the experimental setup. (b) Output-voltage response of the PZT pressure sensor and resistance response of the thermoresistive temperature sensor during repeated strong exhalation. The maximum positive and negative PZT output voltages were +115.37 and −98.35 mV, respectively. The maximum positive voltage corresponded to only 13.9% of the 830 mV signal measured during the face-mask-mounted respiration experiment shown in Figures 5c–d. This result indicates that direct airflow alone cannot account for the high PZT voltage observed in the face-mask experiment and supports the conclusion that face-mask deformation is the primary source of the signal.

Just Accepted

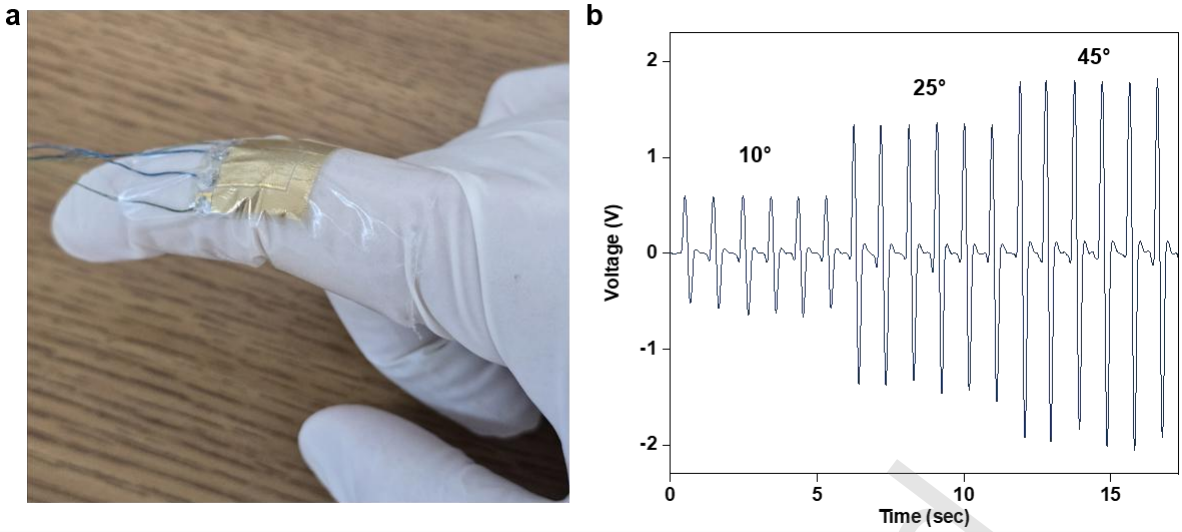


Figure S7 Bending-induced piezoelectric response of the f-MHE. The f-MHE was attached to the dorsal surface of an index finger covered with a latex glove, and the finger was bent downward to angles of approximately 10°, 25°, and 45°. (a) Photograph of the experimental setup. (b) PZT output-voltage responses during repeated bending and straightening cycles at bending angles of approximately 10°, 25°, and 45°. The positive peak voltage increased from 0.594 ± 0.004 V at approximately 10° to 1.346 ± 0.010 V at approximately 25° and 1.799 ± 0.015 V at approximately 45°. The PZT peak voltage of approximately 830 mV measured during the face-mask-mounted respiration experiment shown in Figures 5c–d falls between the values obtained at bending angles of approximately 10° and 25°, supporting the conclusion that deformation-induced bending of the face mask substantially contributed to the measured PZT signal.

Just Accepted

Note 1. Theoretical calculation of R_{ref} used in Equation (1)

1. Geometrical dimensions and material properties of the Au/Cr micropatterns

The temperature sensor consists of Au and Cr layers, which are electrically connected in parallel and have the same length and width.

1) Geometrical dimensions

- Length, $L = 700\,\text{mm}$
- Width, $w = 100\,\mu\text{m}$
- Au thickness, $t_{Au} = 100\,\text{nm}$
- Cr thickness, $t_{Cr} = 10\,\text{nm}$

2) Resistivity at T_{ref} (25 °C)

- $\rho_{Au} = 2.44 \times 10^{-8}\,\Omega \cdot \text{m}$
- $\rho_{Cr} = 1.3 \times 10^{-7}\,\Omega \cdot \text{m}$

2. Resistance of individual layers

The resistance of a metallic layer is calculated using Eq. (S1):

$$R = \frac{\rho L}{wt} \tag{S1}$$

Substituting the geometrical dimensions and resistivity values for the Au and Cr layers into Eq. (S1), the resistance of each layer is calculated to be $R_{Au} = 1708\,\Omega$ and $R_{Cr} = 91000\,\Omega$.

3. Effective resistance of the Au/Cr micropatterns

Since the Au and Cr layers are electrically connected in parallel, the effective resistance R_{ref} of the Au/Cr micropatterns can be calculated using Eq. (S2):

$$\frac{1}{R_{ref}} = \frac{1}{R_{Au}} + \frac{1}{R_{Cr}} = \frac{1}{1708} + \frac{1}{91000} = 5.965 \times 10^{-4} \tag{S2}$$

Therefore, the effective resistance R_{ref} is calculated to be 1676.9 Ω.

Just Accepted

Note 2. Theoretical calculation of α used in Equation (1) and temperature sensitivity

1. Conductance-based formulation

For a metallic layer i, the temperature-dependent resistivity is described by the linear temperature coefficient of resistance (TCR, α) model:

$$\rho_i(T) = \rho_{i0}(1 + \alpha_i \Delta T) \tag{S3}$$

The conductance of layer i is given by:

$$G_i(T) = \frac{wt_i}{L\rho_i(T)} = \frac{wt_i}{L\rho_{i0}(1+\alpha_i \Delta T)} \tag{S4}$$

Define the reference conductance at T_0:

$$G_{i0} = \frac{wt_i}{L\rho_{i0}} \tag{S5}$$

Thus, the temperature-dependent conductance is:

$$G_i(T) = \frac{G_{i0}}{1+\alpha_i \Delta T} \tag{S6}$$

2. First-order approximation for small temperature variations

For $\alpha_i \Delta T \ll 1$, the first-order Taylor approximation gives:

$$\frac{1}{1+\alpha_i \Delta T} \approx 1 - \alpha_i \Delta T \tag{S7}$$

Therefore, the conductance becomes:

$$G_i(T) \approx G_{i0}(1 - \alpha_i \Delta T) \tag{S8}$$

3. Effective TCR α_{tot} of parallel metallic layers

Since the layers are connected in parallel, the total conductance $G_{tot}(T)$ is the sum of individual conductances:

$$G_{tot}(T) = \sum_i G_i\,(T) \tag{S9}$$

Substituting the first-order approximation:

$$G_{tot}(T) = \sum_i G_{i0} - \Delta T \sum_i (\, G_{i0}\alpha_i) \tag{S10}$$

Using the TCR definition:

$$\alpha_{tot} = \frac{1}{R_0}\frac{dR}{dT} = -\frac{1}{G_0}\frac{dG_{tot}}{dT} \tag{S11}$$

Thus, α_{tot} is:

$$\alpha_{tot} = \frac{\sum_i G_{i0}\,\alpha_i}{\sum_i G_{i0}} \tag{S12}$$

Therefore, the effective TCR α_{tot} of parallel metallic layers corresponds to a conductance-weighted average of individual TCR values.

4. Numerical evaluation for the Au/Cr bilayer

The conductance is proportional to the thickness and inversely proportional to resistivity:

Just Accepted

$$G_{i0} \propto \frac{t_i}{\rho_{i0}} \tag{S13}$$

we obtain:

$$\frac{t_{Au}}{\rho_{Au}} = 4.098 \tag{S14}$$

$$\frac{t_{Cr}}{\rho_{Cr}} = 0.07692 \tag{S15}$$

Total proportional conductance is calculated to be 4.17492.
Therefore, α_{tot} is:

$$\alpha_{\text{tot}} = \frac{4.098}{4.17492} \cdot 0.0034 + \frac{0.07692}{4.17492} \cdot 0.0004 \approx 0.0033 \tag{S16}$$

5. Temperature sensitivity of the sensor

For a temperature increase of $\Delta T = 1°C$, the change in resistance is:

$$\Delta R = R_{ref}\alpha_{tot}\Delta T = 1676.9 \times 0.0033 \approx 5.53\,\Omega \tag{S17}$$

Therefore, the temperature sensitivity is:

$$\frac{dR}{dT} \approx 5.53\,\Omega\,°\text{C}^{-1} \tag{S18}$$

Just Accepted